中国激光

基于径向偏振光的波片参数测量方法

唐凡春[1,2]，步扬[1,2*]，吴芳[1,2]，王向朝[1]

[1]中国科学院上海光学精密机械研究所信息光学与光电技术实验室，上海 201800；
[2]中国科学院大学，北京 100049

摘要　提出了一种利用径向偏振光同时测量波片相位延迟量和快轴方位角的方法。水平线偏振光通过涡旋半波片后生成径向偏振光，然后用径向偏振光照射被测波片。由于径向偏振光具有空间非均匀分布的偏振特性，对单次检偏后采集的光强分布依次进行 Radon 变换和最小二乘拟合，可得到强度调制曲线。最后对强度调制曲线进行傅里叶分析，就可计算得到被测波片的相位延迟量和快轴方位角。实验结果表明，当波片的快轴与水平方向的夹角为 45° 时，消色差 1/4 波片和 808 nm 零级 1/4 波片的相位延迟量和快轴方位角的测量标准差小于 0.03°。该方法测量装置简单，测量过程无需转动器件，测量快速方便且测量精度高。

关键词　测量；相位延迟量；快轴方位角；径向偏振；波片

中图分类号　O436.3　　　**文献标志码**　A　　　　　　　　　　　**DOI**：10.3788/CJL202249.1704006

1　引　　言

波片是一种基于晶体双折射特性的偏振光学元件，它能改变入射光场的偏振态[1]，被广泛应用于精密测量、奇点光学和光通信等领域[2-5]。相位延迟量和快轴方位角是波片的两个关键参数。精确测量波片的这两个参数对波片的应用具有重要意义。目前，波片参数的测量方法主要有光弹调制法[6-7]、激光分频法[8]、旋转器件法[9-11]、外差干涉法[12-13]、有限元分析法[14]等。现有方法可以满足测量需求，但在使用中存在不足。例如光弹调制法和外差干涉法可以高精度地测量波片的相位延迟量和快轴方位角，但它们需要复杂的调制信号装置或者干涉装置，且信号处理过程也相当复杂[6, 12-13]；激光分频法无法准确测量波片的快轴方位角[8]；旋转器件法在测量过程中需要旋转偏振片多次以获取不同出射光的强度信息，测量繁琐、耗时且测量过程中器件的旋转和光强的波动会带来测量误差[9]。

不同于线偏振光场、圆偏振光场及椭圆偏振光场等空间偏振均匀分布的光场，矢量光具有空间变化的非均匀偏振分布[15-16]，例如径向偏振矢量光在横截面内任一点的偏振态都沿径向分布。利用矢量光独特的偏振分布的特性，无需旋转偏振器件，在矢量光单次通过被测样品后就可以同时实现不同的空间调制。基于上述优点，矢量光在偏振测量领域得到越来越多的应用[17-18]。

本文提出了一种基于径向偏振光的可以同时测量波片相位延迟量和快轴方位角的方法。该测量方法利用涡旋半波片生成的径向偏振光垂直入射被测波片，基于径向偏振光空间变化的偏振分布特性，探测器只需单次采集检偏后的光强分布图，通过对光强分布图进行 Radon 变换和傅里叶分析，就可以计算得到被测波片的相位延迟量和快轴方位角。该方法可以明显简化测量装置，减少测量步骤。

2　测量原理与实验方案

2.1　测量原理

图 1 所示为利用径向偏振光测量波片相位延迟量和快轴方位角的原理示意图。以水平方向为 x 轴，竖直方向为 y 轴，入射光的传播方向为 z 轴，被测波片的快轴方向与 x 轴方向的夹角为 β，检偏器的透光轴沿竖直方向。入射光为径向偏振光，其垂直入射被测波片，经过检偏器后被电荷耦合元件（CCD）采集。该测量方法的基本原理可用 Mueller 矩阵和 Stokes 矢量来分析：
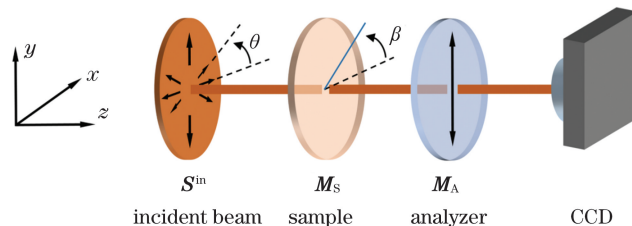

图 1　测量原理示意图

Fig. 1　Schematic of measurement principle

$$S^{\mathrm{out}} = M_{\mathrm{A}} \cdot M_{\mathrm{S}} \cdot S^{\mathrm{in}}, \tag{1}$$

式中：$S^{\mathrm{in}} = \begin{bmatrix} S_0^{\mathrm{in}}, & S_1^{\mathrm{in}}, & S_2^{\mathrm{in}}, & S_3^{\mathrm{in}} \end{bmatrix}^{\mathrm{T}}$ 和 $S^{\mathrm{out}} = \begin{bmatrix} S_0^{\mathrm{out}}, S_1^{\mathrm{out}}, S_2^{\mathrm{out}}, S_3^{\mathrm{out}} \end{bmatrix}^{\mathrm{T}}$ 分别是入射光和出射光的 Stokes 矢量，其中 S_0、S_1、S_2、S_3 为 Stokes 矢量的分

量；T 是矩阵转置符号。入射光为径向偏振光，该光束在其横截面上具有轴对称的偏振态分布[15]，其 Stokes 矢量为 $[1,\cos(2\theta),\sin(2\theta),0]^{\mathrm{T}}$，其中 θ 为方位角[19]。检偏器和被测波片的 Mueller 矩阵分别为

$$M_{\mathrm{A}} = \frac{1}{2} \begin{bmatrix} 1 & -1 & 0 & 0 \\ -1 & 1 & 0 & 0 \\ 0 & 0 & 0 & 0 \\ 0 & 0 & 0 & 0 \end{bmatrix}, \tag{2}$$

$$M_{\mathrm{S}} = \begin{bmatrix} 1 & 0 & 0 & 0 \\ 0 & \cos^2(2\beta)+\cos\delta\,\sin^2(2\beta) & (1-\cos\delta)\sin(2\beta)\cos(2\beta) & -\sin\delta\sin(2\beta) \\ 0 & (1-\cos\delta)\sin(2\beta)\cos(2\beta) & \sin^2(2\beta)+\cos\delta\cos^2(2\beta) & \sin\delta\cos(2\beta) \\ 0 & \sin\delta\sin(2\beta) & -\sin\delta\cos(2\beta) & \cos\delta \end{bmatrix}, \tag{3}$$

式中：δ 和 β 分别为被测波片的相位延迟量和快轴方位角。根据式（1）～（3），可得出射光的 Stokes 矢量 S^{out}，CCD 采集的光强 $I(\theta)$ 与 S_0^{out} 成正比，可得

$$I(\theta) \propto S_0^{\mathrm{out}} = \frac{1}{2} - \frac{1}{2}\left[\cos^2(2\beta)+\cos\delta\sin^2(2\beta)\right]\cos(2\theta) - \frac{1}{2}\left[\cos(2\beta)\sin(2\beta)-\cos\delta\cos(2\beta)\sin(2\beta)\right]\sin(2\theta). \tag{4}$$

式（4）表明，$I(\theta)$ 是方位角 θ 的空间傅里叶级数，周期为 2π，利用傅里叶分析可以得到相关系数。在进行傅里叶分析前需要对 $I(\theta)$ 归一化处理：

$$\begin{cases} a_0 = \dfrac{1}{2\pi}\displaystyle\int_0^{2\pi} I(\theta)\mathrm{d}\theta = \dfrac{1}{2} \\[2mm] a_1 = \dfrac{1}{\pi}\displaystyle\int_0^{2\pi} I(\theta)\cos(2\theta)\mathrm{d}\theta = -\dfrac{1}{2}\left[\cos^2(2\beta)+\cos\delta\sin^2(2\beta)\right] \\[2mm] a_2 = \dfrac{1}{\pi}\displaystyle\int_0^{2\pi} I(\theta)\sin(2\theta)\mathrm{d}\theta = -\dfrac{1}{2}\left[\cos(2\beta)\sin(2\beta)-\cos\delta\cos(2\beta)\sin(2\beta)\right] \end{cases}, \tag{5}$$

式中：a_0、a_1、a_2 为傅里叶级数的系数。

利用式（5）求解得到的傅里叶级数的系数，可得被测波片的 δ 和 β' 的值分别为

$$\begin{cases} \delta = \arccos\left[1 - \dfrac{(2a_1+1)^2+(2a_2)^2}{2a_1+1}\right] \\[2mm] \beta' = \dfrac{1}{2}\arctan\left(-\dfrac{2a_1+1}{2a_2}\right) \end{cases}, \tag{6}$$

式中：β' 为代入 a_1 和 a_2 数值后 β 的初步计算值。从纯数学角度来看，式（6）中 $a_1 = -\dfrac{1}{2}$ 和 $a_2 = 0$ 没有被定义，即当式（5）中 β 为 0°、90°和 180°时，式（6）的 δ 和 β' 无法被求解。这时需要将波片的快轴旋转至合适角度。将计算得到的 a_1 和 a_2 代入式（6）中，可直接得到波片的 δ。波片的快轴方位角 β 可通过如下判断得到：1）当 $2a_1+1 \leqslant \dfrac{1}{2}$，$a_2 < 0$ 时，$\beta = \beta'$；2）当 $2a_1+1 > \dfrac{1}{2}$，$a_2 \geqslant 0$ 时，$\beta = \beta'+90°$；3）当 $2a_1+1 \geqslant \dfrac{1}{2}$，$a_2 < 0$ 时，$\beta = \beta'+90°$；4）当 $2a_1+1 < \dfrac{1}{2}$，$a_2 \geqslant 0$ 时，$\beta = \beta'+180°$。可见，只要对采集到的光强分布图进行处理以得到 a_1 和 a_2 的数值，即可快速求解被测波片的相位延迟量和

快轴方位角。

2.2　实验方案

实验装置示意图如图 2 所示，光源为宽带白光发光二极管（LED），其输出光谱范围为 400～700 nm。LED 光源通过平凸透镜（焦距为 50 mm）和带通滤光器（带宽为 1 nm@632.8 nm）后，生成中心波长为 632.8 nm 的准直且近似均匀分布的红光。起偏器（P1）和检偏器（P2）都是薄膜偏振片，其消光比大于 5000∶1，P1 的透光轴沿水平方向，P2 的透光轴沿竖直方向。涡旋半波片（VR）在光阑上对波长为 633 nm 的光场具有均匀的 90°相位延迟，其快轴围绕其中心连续旋转，能将经过的线偏振光转换为矢量光场。红光通过 P1 和 VR 后生成径向偏振光，然后垂直入射在被测波片上。实验中对两块波片（WP）进行了测量，波片 WP1 为 350～850 nm 波段的消色差 1/4 波片，其在 633 nm 处标定的相位延迟量为 87.04°，波片 WP2 为 808 nm 波长处的零级 1/4 波片，其在 633 nm 处标定的相位延迟量为 116.91°。两块波片的相位延迟量精度都为 1.2°，被测波片的安装座旋转精度约为 0.08°。CCD 相机用来采集经检偏器 P2 调制后的光强分布图，最后通过处理采集的光强分布图可计算得到被测波片的相位延迟量和快轴方位角。
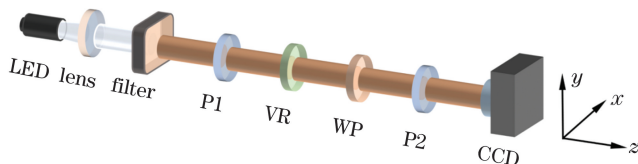
图 2 实验装置示意图

Fig. 2 Schematic of experimental setup

以被测波片标定的快轴方向作为参考，该快轴方向相对水平方向的夹角为标定的快轴方位角（nominal fast axis azimuth，NFAA）。实验过程中以 NFAA 为基准旋转被测波片，使 NFAA 从 5°变至 180°，每间隔 5°用 CCD 采集一次光强分布图。当被测波片 WP1 的 NFAA 为 60°时，CCD 采集的光强分布图如图 3(a)所示，光强呈沙漏形分布。以图 3(a)所示图像中心为原点，截取半径为光强分布图半径的 30%～60%的圆环

区域进行 Radon 变换，截取的圆环强度分布如图 3(b)所示。从圆环图像的中心开始，沿所有方位角 θ，利用 Radon 变换对圆环强度值进行线积分，从而得到 $0～2\pi$ 范围的积分曲线，然后对积分曲线进行归一化处理，得到光强调制曲线 $I'(\theta)$[20]。考虑到 CCD 采集的光强分布图中存在明显噪点，为了降低 CCD 噪声对测量结果的影响，对 Radon 变换直接得到的光强调制曲线 $I'(\theta)$ 进行最小二乘拟合，得到光强调制曲线 $I(\theta)$。截取圆环区域进行处理是因为考虑到实验过程中图像中心和边缘的调制效果差，测量精度低，所以需要从光强分布图中截取调制效果良好的圆环区域。需要对 Radon 变换后得到的强度调制曲线进行归一化处理，得到的强度调制曲线 $I'(\theta)$ 与拟合的光强调制曲线 $I(\theta)$ 如图 3(c)所示。利用强度调制曲线 $I(\theta)$，根据式(5)、(6)可以计算得到被测波片的相位延迟量和快轴方位角。
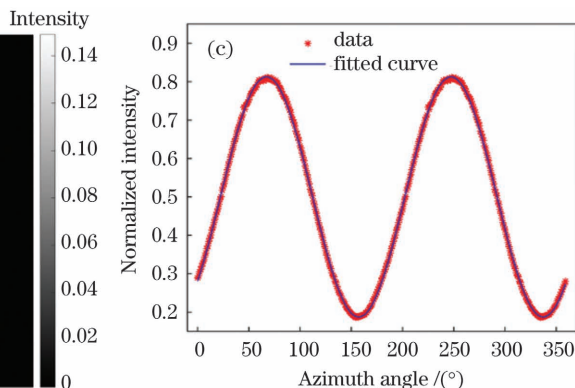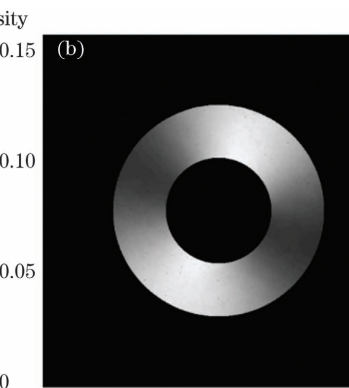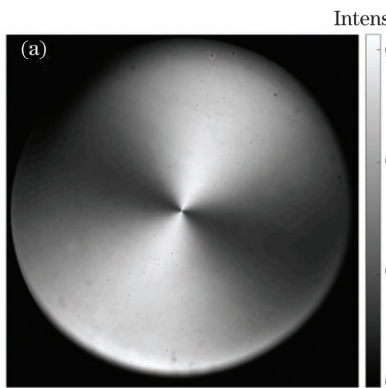

图 3 NFAA 为 60°时的实验结果。(a)沙漏形光强分布图；(b)从图 3(a)中截取的圆环；(c)从图 3(b)中得到的归一化强度调制曲线与拟合的强度调制曲线

Fig. 3 Experimental results when NFAA is 60°. (a) Intensity pattern with hourglass shape; (b) ring taken from Fig. 3(a); (c) normalized intensity modulation curve and fitted intensity modulation curve obtained from Fig.3(b)

3 误差分析

根据实验装置的结构可知，VR 的快轴分布误差、偏振器的对准误差和 CCD 的噪声等因素都会影响测量结果的准确性。

3.1 VR 的零度快轴误差分析

VR 的快轴方向是空间变化的，VR 的零度快轴在定制和装配过程中可能会偏离真实的零度角。当 VR

的零度快轴出现 $\Delta\theta$ 偏离误差时，水平线偏振光通过 VR 后将会生成其他的矢量偏振光场，其 Stokes 矢量为 $[1,\cos[2(\theta+\Delta\theta)],\sin[2(\theta+\Delta\theta)],0]^{\mathrm{T}}$。为了分析 VR 的零度快轴出现偏离误差时对测量结果的影响，设定被测波片的相位延迟量为 87.04°，NFAA 设置在 5°～85°和 95°～175°区间，对零度快轴不存在偏离误差和存在 1°偏离误差的情况分别进行仿真计算。两者的仿真计算结果如图4所示。从图4(a)可知，当
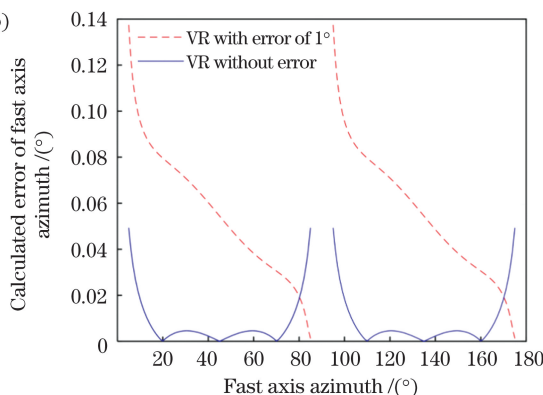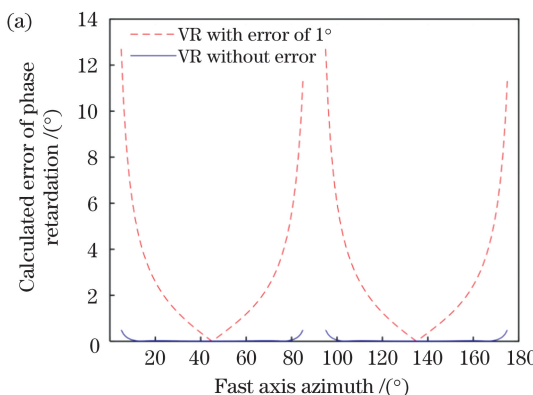

图 4 考虑 VR 零度快轴误差时的仿真计算结果。(a)相位延迟量误差；(b)快轴方位角误差

Fig. 4 Simulation results considering error of VR zero-degree fast axis. (a) Error of phase retardation; (b) error of fast axis azimuth

VR 的零度快轴存在 1°偏离误差时,其对被测波片相位延迟量的计算结果存在很大影响。在 VR 的零度快轴无误差的情况下,仿真计算的相位延迟量与设定值 87.04°的最大误差为 0.07°。在零度快轴存在 1°偏离误差的情况下,当 NFAA 在 30°~60°和 120°~150°区间时,相位延迟量的仿真计算误差较小,与设定值的最大误差为 1.24°。其中,当 NFAA 为 45°和 135°时,仿真计算的误差最小;当 NFAA 在其他角度区间时,相位延迟量的仿真计算误差较大,且 NFAA 越接近 0°、90°和 180°,仿真计算误差越大。从图 4(b)中可以看出,当 VR 的零度快轴存在 1°偏离误差时,其对被测波片快轴方位角的计算结果影响较小,快轴方位角的最大仿真计算误差小于 0.14°。考虑到 VR 的零度快轴的偏离误差对被测波片参数测量结果的影响,实验过

程中需要确定 VR 的零度快轴存在的偏离误差,并在求解波片参数时对偏离误差进行补偿。在测量被测波片参数过程中,使其 NFAA 处于 30°~60°或者 120°~150°区间,可最大程度降低涡旋半波片的零度快轴偏离误差对测量结果的影响。

3.2　系统误差分析

除了光源的均匀性和 VR 的零度快轴的偏离误差外,偏振器的消光比、CCD 的噪声、环境温度变化等其他因素也会带来相应的误差,它们综合影响着测量结果。本文提出的测量方法是对 CCD 采集的光强分布图进行 Radon 变换和傅里叶分析,从而得到式(5)中的 a_1 和 a_2,然后利用 a_1 和 a_2 求解得到相位延迟量 δ 和快轴方位角 β 的值。假设 a_1 和 a_2 对测量结果的影响相同,那么 a_1 和 a_2 对 δ 和 β 的误差影响[21]为

$$\frac{\mathrm{d}\delta}{\mathrm{d}a_n} = \frac{1}{\dfrac{\mathrm{d}a_n}{\mathrm{d}\delta}} = \frac{1}{\left| \begin{pmatrix} \dfrac{\partial a_1}{\partial \delta} \\ \dfrac{\partial a_2}{\partial \delta} \end{pmatrix} \right|} = \frac{1}{\sqrt{\left(\dfrac{\partial a_1}{\partial \delta}\right)^2 + \left(\dfrac{\partial a_2}{\partial \delta}\right)^2}} = \frac{2}{|\sin\delta \cdot \sin(2\beta)|}, \tag{7}$$

$$\frac{\mathrm{d}\beta}{\mathrm{d}a_n} = \frac{1}{\dfrac{\mathrm{d}a_n}{\mathrm{d}\beta}} = \frac{1}{\left| \begin{pmatrix} \dfrac{\partial a_1}{\partial \beta} \\ \dfrac{\partial a_2}{\partial \beta} \end{pmatrix} \right|} = \frac{1}{\sqrt{\left(\dfrac{\partial a_1}{\partial \beta}\right)^2 + \left(\dfrac{\partial a_2}{\partial \beta}\right)^2}} = \frac{1}{\sqrt{2}\,(1-\cos\delta)}, \tag{8}$$

式中:$n=1,2$。

根据式(7)可知,当 δ 为 0°或者 180°的整数倍时,δ 的测量值对误差敏感;当 β 为 0°或者 90°的整数倍时,δ 的测量值同样对误差敏感。根据式(8)可知,对于快轴方位角 β,当 δ 在 0°~180°区间时,δ 的值越大,β 的测量结果受误差的影响越小。综合分析式(7)、(8)可知,该测量方法不适合测量相位延迟量约为 0°或者 180°的整数倍的波片,测量时被测波片的快轴方位角应该避免为 0°或者 90°的整数倍。

4　实验测量结果

4.1　未插入被测波片

为了对 VR 的零度快轴的偏离误差进行补偿,需要知道 VR 的零度快轴的偏离误差。当 VR 的零度快轴存在偏离误差 $\Delta\theta$ 时,水平线偏振光通过 VR 后将会生成矢量偏振光场,其 Stokes 矢量为 $[1,\cos[2(\theta+\Delta\theta)],\sin[2(\theta+\Delta\theta)],0]^{\mathrm{T}}$。未插入被测波片时,矢量光经过检偏器 P2 后被 CCD 采集,这时

被测样品为空气,其 Mueller 矩阵为单位矩阵:

$$\boldsymbol{M} = \begin{bmatrix} 1 & 0 & 0 & 0 \\ 0 & 1 & 0 & 0 \\ 0 & 0 & 1 & 0 \\ 0 & 0 & 0 & 1 \end{bmatrix}_{\mathrm{air}} \, 。 \tag{9}$$

根据式(3),这时 CCD 采集的光强 $I(\theta)$ 为

$$I(\theta) \propto S_0^{\mathrm{out}} = \frac{1}{2} - \frac{1}{2}\cos[2(\theta+\Delta\theta)] \, 。 \tag{10}$$

未插入被测波片时的实验结果如图 5 所示。图 5(a)是实验中未插入被测波片时采集的光强分布图。从图 5(a)中截取半径为光强分布图半径的 30%~60% 的圆环区域,得到的圆环强度分布如图 5(b)所示。对图 5(b)中的圆环进行 Radon 变换,然后进行归一化处理,可以得到强度调制曲线,对归一化的强度调制曲线进行最小二乘拟合,结果如图 5(c)所示。通过拟合,确定 VR 的零度快轴存在的偏离误差 $\Delta\theta$ 为 -2.03°,其 95% 置信区间为 ±0.07°。

确定偏离误差 $\Delta\theta$ 后,将式(5)修正为

$$\begin{cases} a_0 = \dfrac{1}{2\pi}\displaystyle\int_0^{2\pi} I(\theta)\,\mathrm{d}\theta = \dfrac{1}{2} \\[3mm] a_1 = \dfrac{1}{\pi}\displaystyle\int_0^{2\pi} I(\theta)\cos[2(\theta+\Delta\theta)]\,\mathrm{d}\theta = -\dfrac{1}{2}\left[\cos^2(2\beta) + \cos\delta\sin^2(2\beta)\right] \\[3mm] a_2 = \dfrac{1}{\pi}\displaystyle\int_0^{2\pi} I(\theta)\sin[2(\theta+\Delta\theta)]\,\mathrm{d}\theta = -\dfrac{1}{2}\left[\cos(2\beta)\sin(2\beta) - \cos\delta\cos(2\beta)\sin(2\beta)\right] \end{cases} \, 。 \tag{11}$$
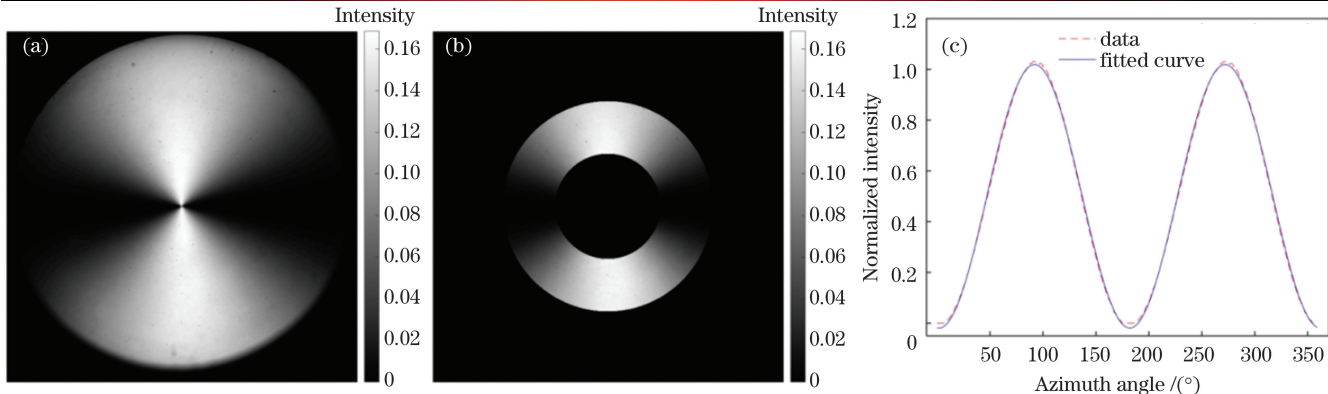
图 5 未插入被测波片时的实验结果。(a)沙漏形光强分布图;(b)从图 5(a)中截取的圆环;(c)从图 5(b)中得到的归一化强度调制曲线与拟合的强度调制曲线

Fig. 5 Experimental results before inserting wave plate to be measured. (a) Intensity pattern with hourglass shape; (b) ring taken from Fig. 5(a); (c) normalized intensity modulation curve and fitted intensity modulation curve obtained from Fig.5(b)

在式(11)中,$\Delta\theta$ 的单位为弧度。利用式(6)求解得到被测波片的相位延迟量和快轴方位角,极大地减小了 VR 的快轴分布误差对测量结果的影响。

4.2 插入被测波片

首先插入被测消色差 1/4 波片 WP1,将 WP1 初始 NFAA 设置为 5°,然后旋转被测波片,每间隔 5°用 CCD 采集检偏后的光强分布图。根据 2.2 节中的处理步骤,对采集到的光强分布图进行处理,得到拟合的光强调制曲线,然后根据式(6)、(11)计算得到被测波片的相位延迟量和快轴方位角。插入消色差 1/4 波片 WP1 后的实验测量结果如图 6 所示。从图 6(a)中可以看出,当被测波片 NFAA 在 0°、90°和180°附近时,相位延迟量的测量值波动较大,当 NFAA 在 45°和135°附近时,相位延迟量的测量值接近标定值 87.04。当 NFAA 在 30°~60°和120°~150°区间时,相位延迟量的测量平均值和标准

差分别为 87.30°和 0.26°。从图 6(b)中可以看出,快轴方位角在整个测量区间基本呈线性分布,快轴方位角的测量值与标定值之间偏差的平均值和标准差分别为 3.20°和 0.68°。根据 3.2 节的分析可知,当被测波片 NFAA 在 45°和135°附近时,测量精度最高。因此,为了进一步验证测量方案的准确性和稳定性,设置 NAFF 为 45°,对相位延迟量和快轴方位角进行了 10 次测量。测量结果如表 1 所示,相位延迟量的测量平均值和标准差分别为 87.33°和 0.01°,与设定值的偏差为 0.29°;快轴方位角的测量平均值和标准差分别为 48.01°和 0.01°。被测波片 WP1 的实验结果表明,当 NFAA 在 30°~60°和 120°~150°区间,尤其是在 45°附近时,相位延迟量的测量结果具有较高的测量精度和稳定性;而对于快轴方位角,精确测量区间则更大,只有当 NFAA 在 0°、90°和180°附近时,其测量误差会较大。
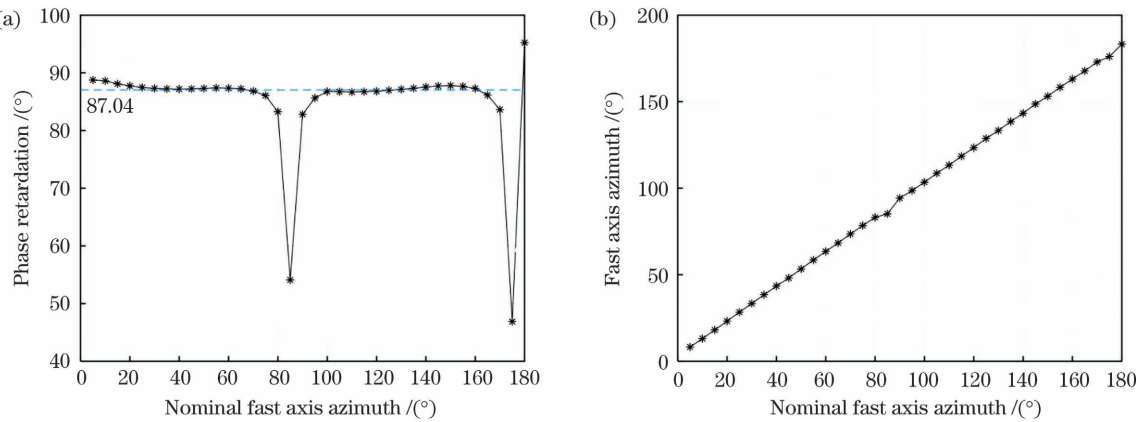

图 6 插入消色差 1/4 波片后的测量结果。(a)相位延迟量;(b)快轴方位角

Fig. 6 Measurement results after inserting achromatic quarter-wave plate. (a) Phase retardation; (b) fast axis azimuth

插入被测消色差 1/4 波片 WP1 后的测量结果表明,当被测波片 NFAA 在 0°、90°和180°附近时,相位延迟量和快轴方位角的测量误差都较大。这是因为当被测波片快轴与检偏器透光方向平行或者垂直时,在径向偏振光入射被测波片后的光强调制过程中,检偏器擦除了被测波片的参数信息。从式(4)中也可以看出,当被测波片的快轴方位角为 0°、90°和180°时,检偏

后的光强分布 $I(\theta)\propto 1-\cos(2\theta)$,这时检偏后的光强分布与被测波片的 δ 和 β 无关,因此无法准确测量出这两个参数。

为了进一步验证本测量方法的实用价值,实验中还测量了 808 nm 零级 1/4 波片 WP2。当 NFAA 在 30°~60°和 120°~150°区间时,相位延迟量的测量平均值和标准差分别为 116.60°和 0.59°。快轴方位角

的测量值与标定值之间偏差的平均值和标准差分别为 0.85° 和 0.26°。同时在其 NFAA 在 45° 时进行了 10 次测量,测量结果如表 1 所示。相位延迟量的测量平

均值和标准差分别为 117.04° 和 0.03°,与设定值的偏差为 0.13°;快轴方位角的测量平均值和标准差分别为 45.64° 和 0.01°。

表 1　NFAA 为 45° 时相位延迟量和快轴方位角的多次测量结果

Table 1　Multiple measurement results of phase retardation and fast axis azimuth when NFAA is 45°

Sample	δ /(°)		β /(°)	
	Average	Standard deviation	Average	Standard deviation
Achromatic quarter-wave plate	87.33	0.01	48.05	0.01
Zero-order quarter-wave plate (@808 nm)	117.04	0.03	45.64	0.01

5　结　　论

提出了一种基于径向偏振光同时测量波片相位延迟量和快轴方位角的方法。该方法利用径向偏振光空间变化的偏振分布特性,对单次成像的光强分布图进行 Radon 变换,并基于最小二乘拟合,得到随方位角变化的强度调制曲线,最后对强度调制曲线进行傅里叶分析,就可计算得到被测波片的相位延迟量和快轴方位角。理论分析表明,当被测波片的相位延迟量为 0° 或者 180° 的整数倍时,或者当被测波片的快轴方向与水平方向的夹角为 0° 或者 90° 的整数倍时,波片参数测量结果对误差敏感。实验中对两块波片进行了测量,实验结果表明,当被测波片的快轴与水平方向的夹角在 30°~60° 和 120°~150° 区间,尤其是在 45° 附近时,通过单次成像就可以测量得到波片参数,且测量结果具有较高的准确性和稳定性。该方法有以下优点:1) 测量装置简单,减少了误差源;2) 测量过程只需单次成像,无需转动器件,测量快速方便;3) 校准了涡旋半波片的快轴分布误差,通过最小二乘拟合降低了 CCD 相机噪声对测量结果的影响。后续将研究被测波片的全局双折射分布测量问题以及线偏振器的消光比和光源的均匀性等因素对测量结果的影响。

参 考 文 献

[1] Goldstein D H. Polarized light [M]. 3rd ed. Florida: CRC Press, 2017: 100-103.

[2] Zhu R G, Zhou J J, Li B, et al. Measurement error caused by quarter-wave plate in the dynamic interferometer: theory and correction method [J]. Optics Communications, 2022, 502: 127406.

[3] Manthalkar A, Nape I, Bordbar N T, et al. All-digital Stokes polarimetry with a digital micromirror device [J]. Optics Letters, 2020, 45(8): 2319-2322.

[4] Liu Z X, Liu Y Y, Ke Y G, et al. Generation of arbitrary vector vortex beams on hybrid-order Poincaré sphere [J]. Photonics Research, 2016, 5(1): 15-21.

[5] Wang J. Advances in communications using optical vortices [J]. Photonics Research, 2016, 4(5): B14-B28.

[6] Zeng A J, Li F Y, Zhu L L, et al. Simultaneous measurement of retardance and fast axis angle of a quarter-wave plate using one photoelastic modulator [J]. Applied Optics, 2011, 50(22): 4347-4352.

[7] 张瑞, 陈媛媛, 景宁, 等. 基于双弹光差频调制的中红外波片相位延迟高精度测量 [J]. 光学学报, 2019, 39(3): 0312002.

Zhang R, Chen Y Y, Jing N, et al. High-precision measurement of mid-infrared waveplate phase retardation based on dual photoelastic difference frequency modulation [J]. Acta Optica Sinica, 2019, 39(3): 0312002.

[8] Liu W X, Liu M, Zhang S L. Method for the measurement of phase retardation of any wave plate with high precision [J]. Applied Optics, 2008, 47(30): 5562-5569.

[9] Williams P A, Rose A H, Wang C M. Rotating-polarizer polarimeter for accurate retardance measurement [J]. Applied Optics, 1997, 36(25): 6466-6472.

[10] Wang W, Chen J Z. Simple method for simultaneous determination of the phase retardation and fast axis of a wave plate [J]. Optik, 2013, 124(20): 4359-4363.

[11] 彭建国, 袁沐, 金振宇, 等. 基于双光束检偏的波片测量系统 [J]. 光学学报, 2020, 40(9): 0912002.

Peng J G, Yuan S, Jin Z Y, et al. Accurate parameter measurement of wave plate based on the dual-beam polarization analyzer configuration [J]. Acta Optica Sinica, 2020, 40(9): 0912002.

[12] Chiu M H, Chen C D, Su D C. Method for determining the fast axis and phase retardation of a wave plate [J]. Journal of the Optical Society of America A, 1996, 13(9): 1924-1929.

[13] Lo Y L, Lai C H, Lin J F, et al. Simultaneous absolute measurements of principal angle and phase retardation with a new common-path heterodyne interferometer [J]. Applied Optics, 2004, 43(10): 2013-2022.

[14] 刘志帆, 蔡燕民, 步扬, 等. 基于有限元分析方法的深紫外波段熔石英应力双折射分析 [J]. 光学学报, 2021, 41(12): 1226001.

Liu Z F, Cai Y M, Bu Y, et al. Stress birefringence analysis in fused silica at deep ultraviolet waveband based on finite element simulation method [J]. Acta Optica Sinica, 2021, 41(12): 1226001.

[15] Suárez-Bermejo J C, González de Sande J C, Santarsiero M, et al. Mueller matrix polarimetry using full Poincaré beams [J]. Optics and Lasers in Engineering, 2019, 122: 134-141.

[16] de Sande J C G, Piquero G, Santarsiero M. Polarimetry with azimuthally polarized light [J]. Optics Communications, 2018, 410: 961-965.

[17] Zhan Q W. Cylindrical vector beams: from mathematical concepts to applications [J]. Advances in Optics and Photonics, 2009, 1(1): 1-57.

[18] Feng L P, Li Y, Wu S H, et al. All-fiber generation of arbitrary cylindrical vector beams on the first-order Poincaré sphere [J]. Photonics Research, 2020, 8(8): 1268-1277.

[19] Rosales-Guzmán C, Ndagano B, Forbes A. A review of complex vector light fields and their applications [J]. Journal of Optics, 2018, 20(12): 123001.

[20] Gao C, Lei B. Spatially modulated polarimetry based on a vortex retarder and Fourier analysis [J]. Chinese Optics Letters, 2021, 19(2): 021201.

[21] Lane C, Rode D, Rösgen T. Two-dimensional birefringence measurement technique using a polarization camera [J]. Applied Optics, 2021, 60(27): 8435-8444.

Parameter Measurement of Wave Plate Based on Radially Polarized Beams

Tang Fanchun[1,2], Bu Yang[1,2*], Wu Fang[1,2], Wang Xiangzhao[1]

[1] *Laboratory of Information Optics and Opto-Electronic Technology, Shanghai Institute of Optics and Fine Mechanics,
Chinese Academy of Sciences, Shanghai 201800, China;*
[2] *University of Chinese Academy of Sciences, Beijing 100049, China*

Abstract

Objective Wave plates are critical components in several fields, including precision measurement, singularity optics, and optical communication. A wave plate's phase retardation and fast axis azimuth are two key parameters. The precise measurement of these two parameters is of great significance for the use of a wave plate. The methods including photoelastic modulation method, laser frequency division method, rotating device method, heterodyne interference method, and finite element simulation method are used to measure the two parameters. These methods are effective; however, they are not without drawbacks. Vector beams have a spatially inhomogeneous polarized distribution compared to common linearly and circularly polarized beams. The polarization state of radially polarized vector beams, for example, is distributed along the radial direction at any point in the cross-section. Furthermore, all linear polarization states can simultaneously be very useful for measuring the parameters of a wave plate, and as a result, vector beams are gaining popularity in the field of polarimetry.

Methods First, the measurement principle of the proposed method based on the Muller matrix and Stokes vector is described in Fig. 1. Second, formulas for calculating the measured wave plate's phase retardation and fast axis azimuth are developed. Finally, the effects of the vortex retarder (VR) zero-degree fast axis error, charge-coupled device (CCD) noise, and other factors on measurement accuracy are investigated. The experimental setup is constructed based on the measurement principle. The light source in the experiment is a white-light emitting diode, which is transformed into a collimated uniform red light field of 633 nm after passing through a plane-convex lens and a bandpass filter. When the red light passes through the horizontal linear polarizer and the vortex retarder, it produces a radially polarized beam. The radially polarized beam is then passed through a measured wave plate and a vertical linear polarizer. Finally, the intensity distribution is captured by a CCD. The intensity distribution image in Fig. 3(a) shows an hourglass distribution. Since the edges and center of the intensity distribution are typically poorly modulated, the ring area of interest region is intercepted from the image in Fig. 3(a), as illustrated in Fig. 3(b). The Radon transform is adopted to obtain the intensity curve $I'(\theta)$ varying along with the azimuth θ. To reduce the influence of noise from CCD on the measurement results, the intensity curve $I'(\theta)$ is fitted by the least-square fitting method to obtain the intensity curve $I(\theta)$. By using Fourier analysis of the normalized intensity curve $I(\theta)$, the phase retardation and fast axis azimuth of the wave plate can be measured.

Results and Discussions The error analysis shows that a minor error in the vortex retarder's zero-degree fast axis can affect phase retardation measurements; however, it has little effect on the measurement results of fast axis azimuth. Using the nominal fast axis direction of the measured wave plate as a reference, the nominal fast axis azimuth (NFAA) is defined as the angle between the nominal fast axis direction and the horizontal direction . From the error analysis, we can see that measurement results for the phase retardation tend to be inaccurate if measuring a wave plate with phase retardation of 0° or a multiple of 180°. Furthermore, for the same reason, phase retardation measurement results are sensitive to errors when the NFAA of the wave plate is 0° or a multiple of 180°. Before inserting the wave plate to be measured, an experiment is performed without any sample to calculate the deviation of VR's zero-degree fast axis, which can greatly improve measurement accuracy. An achromatic quarter-wave plate is measured in the experiment. The experimental results show that it has the highest measurement accuracy when the NFAA of the measured achromatic quarter-wave plate is in the range near 45° and 135°, but the measured value fluctuates greatly when the NFAA is near 0°, 90°, and 180°. When the NFAA of the measured achromatic quarter-wave plate is in the range of 30°−60°and 120°−150°, the measured average value and standard deviation of the phase retardation are 87.30° and 0.26°, respectively. The average value and standard deviation of the deviation between the measured value and the nominal value of the fast axis azimuth are 3.20° and 0.68°, respectively. To further confirm the accuracy and stability of the measurement scheme, the NFAA is set as 45°, and it is measured 10 times. The measured average value and standard deviation of the phase retardation are 87.33°and 0.01°, respectively, and those of the fast axis azimuth is 48.01° and 0.01°, respectively. To further verify the practical value of this measurement method, a zero-order quarter-wave plate at 808 nm is also

measured. When the NFAA of the measured zero-order quarter-wave plate is in the range of $30°–60°$ and $120°–150°$, the measured average value and standard deviation of the phase retardation are $116.60°$ and $0.59°$, respectively. Moreover, the average value and standard deviation of the deviation between the measured value and the nominal value of the fast axis azimuth are $0.85°$ and $0.26°$, respectively. Multiple measurements are performed when the NFAA is $45°$. The measured average value and standard deviation of phase retardation are $117.04°$ and $0.03°$, respectively, and the measured mean value and standard deviation of fast axis azimuth are $45.64°$ and $0.01°$, respectively.

Conclusions　This paper proposes a method for simultaneously measuring phase retardation and fast axis azimuth of a wave plate using a radially polarized vector beam. In this method, the phase retardation and fast axis azimuth of the measured wave plate can be calculated by Fourier analysis of the intensity modulation curve obtained by the Radon transform and least-square fitting of the recorded light intensity with a snapshot baesd on the spatially variant polarized distribution characteristics of radially polarized beams. The theoretical analysis shows that when the phase retardation of the measured wave plate is $0°$ or a multiple of $180°$ or the angle between the fast axis direction of the measured wave plate and the horizontal direction is $0°$ or a multiple of $90°$, the measurement results are sensitive to errors. Two wave plates are measured in the experiment. The experimental results demonstrate that when the angle between the fast axis and the horizontal direction of the evaluated wave plate is in the range of $30°–60°$ and $120°–150°$, particularly near $45°$, the parameters of the wave plate can be measured by a single snapshot, and the measurement results have good accuracy and stability. The advantages of this method are as follows: first, the error source is reduced since the measuring device is simple; second, the measurement is rapid and convenient since only a single imaging is used in the measurement process and there is no need to rotate the device; and finally, the fast axis distribution error of the vortex retarder is calibrated, and the influence of noise of the CCD camera on the measurement results is reduced by the least-square fitting. However, some aspects require further investigation, such as the measurement of the measured wave plate's global birefringence distribution and the effects of the linear polarizer's extinction ratio and the uniformity of the light source on measurement results.

Key words　measurement; phase retardation; fast axis azimuth; radially polarized beam; wave plate